# Magnetic Stability of Massive Star-forming Clumps in RCW 106

Shohei Tamaoki[1] , Koji Sugitani[1] , Quang Nguyen-Luong[2], Fumitaka Nakamura[3] , Takayoshi Kusune[3] ,
Takahiro Nagayama[4], Makoto Watanabe[5] , Shogo Nishiyama[6], and Motohide Tamura[3,7,8]

[1] Graduate School of Natural Sciences, Nagoya City University, Mizuho-ku, Nagoya 467-8501, Japan
[2] IBM Canada, 120 Bloor Street East, Toronto, ON, M4Y 1B7, Canada
[3] National Astronomical Observatory of Japan, Mitaka, Tokyo 181-8588, Japan
[4] Kagoshima University, 1-21-35 Korimoto, Kagoshima 890-0065, Japan
[5] Department of Applied Physics, Okayama University of Science, 1-1 Ridai-cho, Kita-ku, Okayama 700-0005, Japan
[6] Miyagi University of Education, 149 Aramaki-aza-Aoba, Aobaku, Sendai, Miyagi 980-0845, Japan
[7] Department of Astronomy, The University of Tokyo, 7-3-1, Hongo, Bunkyo-ku, Tokyo, 113-0033, Japan
[8] Astrobiology center of NINS, 2-21-1, Osawa, Mitaka, Tokyo 181-8588, Japan

## Abstract

The RCW 106 molecular cloud complex is an active massive star-forming region where a ministarburst is taking place. We examined its magnetic structure by near-IR polarimetric observations with the imaging polarimeter SIRPOL on the IRSF 1.4 m telescope. The global magnetic field is nearly parallel to the direction of the Galactic plane and the cloud elongation. We derived the magnetic field strength of $\sim$100–1600 $\mu$G for 71 clumps with the Davis–Chandrasekhar–Fermi method. We also evaluated the magnetic stability of these clumps and found that massive star-forming clumps tend to be magnetically unstable and gravitationally unstable. Therefore, we propose a new criterion to search for massive star-forming clumps. These details suggest that the process enhancing the clump density without an increase of the magnetic flux is essential for the formation of massive stars and the necessity for accreting mass along the magnetic field lines.

*Key words:* H II regions – ISM: clouds – ISM: magnetic fields – ISM: structure – stars: formation – stars: massive

## 1. Introduction

Magnetic fields are believed to play an essential role in star formation at all scales because the interstellar medium is generally magnetized (Crutcher 2012). However, whether they play deconstructive or constructive roles in the evolution of stars and molecular clouds is not entirely understood. From the theoretical point of view, magnetic field is a process that can be distinguished in massive and low-mass star formation (see Shu et al. 1987). Magnetic fields in magnetically subcritical clumps support the clumps from collapsing gravitationally under conservation of magnetic flux and therefore only allow the cloud to form low-mass stars with ambipolar diffusion that advances steady and slow instead of massive stars that require drastic collapsing. Conversely, magnetically supercritical ones would generate the high-mass core needed for massive star formation thanks to the onset of relatively rapid contraction.

At a distance of 3.6 kpc (Lockman 1979), the RCW 106 molecular cloud complex is a very active massive star-forming region, so active that it is classified as a ministarburst site. Its 83 pc long structure is located in the Scutum–Centaurus arm and is elongated approximately in the ENE–WSW direction ($\sim$25° from north to east). This $6 \times 10^6 M_\odot$ complex is powered by the giant H II region RCW 106 (Nguyen et al. 2015), one of the largest and brightest H II regions in the Milky Way. The giant H II region RCW 106 hosts a cluster with a mass of $\sim$10$^3 M_\odot$ and Lyman continuum photon emission of $10^{50}$ s$^{-1}$, likely originating from dozens of OB-type stars ($M > 8 M_\odot$) (Lynga 1964) or radio continuum photon emission that is responsible for 54 OB stars (Nguyen et al. 2015). High density tracers such as CS, HCO$^+$, HCN, HNC, and NH$_3$ emission lines revealed a large sample of cold clumps and these clumps coincide with 1.2 mm dust clumps (Mookerjea et al. 2004), which are sites of massive star formation or are gravitationally unstable clumps and potentially forming stars (Bains et al. 2006; Wong et al. 2008; Lo et al. 2009; Lowe et al. 2014).

Although being a famous massive star-forming complex, its magnetic field structure remains unknown. Therefore, we observed the polarized starlight in near-infrared bands using the imaging polarimeter SIRPOL (polarimetry mode of the SIRIUS camera; Kandori et al. 2006) mounted on the Infrared Survey Facility (IRSF) 1.4 m telescope at the South African Astronomical Observatory.

## 2. Observations

### 2.1. Polarimetric Observations with SIRPOL

Magnetic fields can be revealed at near-IR by starlight polarization due to interstellar grain alignment based on radiative processes (see Andersson et al. 2015). Near-IR imaging polarimetry toward RCW 106 was made on 2017 April and May, 2018 January, July, and August with SIRPOL/SIRIUS on IRSF. The camera has simultaneous observation capability at $JHK_s$ bands using three $1024 \times 1024$ HgCdTe arrays, $JHK_s$ filters, and dichroic mirrors (Nagashima et al. 1999; Nagayama et al. 2003). The field of view at each band is $\sim$7′.7 × 7′.7 with a pixel scale of 0″.45. We have observed 54 fields in total. For each field, we obtained 10 dithered exposures, each of 15 s long, at four waveplate angles (0°, 22°.5, 45°, and 67°.5 in the instrumental coordinate system) and repeated it six times. Thus, the total exposure time was 900 s for each waveplate angle. The seeing size ranged from $\sim$1″.5 to 2″.3 at $H$ band. Twilight flat-field images were obtained at the beginning and/or end of the observations. Standard image reduction procedures were applied with IRAF/PyRAF. Aperture photometry was executed at $J$, $H$, and $K_s$, with an aperture radius of $\sim$1 FWHM corresponding to the seeing size. The

2MASS catalog (Skrutskie et al. 2006) was used for photometric/astrometric calibration. Only the sources with photometric measurement errors of less than 0.1 mag were used for analysis. The Stokes parameters were calculated as $I = (I_0 + I_{22.5} + I_{45} + I_{67.5})/2$ and $q = (I_0 - I_{45})/I$, $u = (I_{22.5} - I_{67.5})/I$, where $I_0$, $I_{22.5}$, $I_{45}$, and $I_{67.5}$ are the intensities at four waveplate angles. The Stokes parameters were converted into the equatorial coordinate system $(q', u')$ with a rotation of 105° (Kandori et al. 2006; Kusune et al. 2015). The degree of polarization $P$ and the polarization angle $\theta$ were calculated as $\theta = (1/2)$atan $(u'/q')$ and $P = (q^2 + u^2)^{1/2}$. The errors in polarization ($\Delta P$ and $\Delta \theta$) were derived from the photometric errors. We adopted the measurable polarization limit of ~0.3% (Kandori et al. 2006) and $\Delta P = 0.3\%$ was assigned to the sources of $\Delta P < 0.3\%$. The degrees of polarization were debiased as $P_{\mathrm{debias}} = (P^2 - \Delta P^2)^{1/2}$ (Wardle & Kronberg 1974). Because of the high polarization efficiencies of 95.5% at $J$, 96.3% at $H$, and 98.5% at $K_{\mathrm{s}}$ (Kandori et al. 2006), no particular corrections were applied further.

### 2.2. Archival Data

The *Herschel* Science Archive SPIRE/PACS data were used to obtain the $H_2$ column density map. First, we convolved the 350/250/160 μm images to the 500 μm image resolution, 36″. Then, we derived the spectral energy distribution (SED) at each pixel by SED fitting using the four images described above, in the same way as Konyves et al. (2010). We adopted the dust opacity per unit mass, $\kappa_\nu = 0.1(\nu/1000\,\mathrm{GHz})^\beta$ cm²/g, where $\beta = 2.0$.

We fitted only pixels where signals are detected more than 3 rms in all four bands. The rms was measured around the reference area (R.A.$_{\mathrm{J2000}} = 16{:}19{:}19.64$, decl.$_{\mathrm{J2000}} = -51{:}45{:}36.1$). We obtained a column density ($N_{\mathrm{H_2}}$) map with a higher resolution of 18″ using an equation of $N_{\mathrm{H_2}} = I_\nu/[B_\nu(T_{\mathrm{d}})\kappa_\nu \mu m_{\mathrm{H}}]$, where $I_\nu$ is the 250 μm non-convolved brightness, $B_\nu(T_{\mathrm{d}})$ is the Planck function at the dust temperature $T_{\mathrm{d}}$ derived by the SED fitting (mean: $22.5 \pm 1.9$ K, range: ~15–42 K), $\mu$ is the mean molecular weight of 2.8, and $m_{\mathrm{H}}$ is the hydrogen atom mass. The obtained $N_{\mathrm{H_2}}$, when convolved to the 36″ resolution, is consistent with that of the SED fitting within 10%.

We also use the $^{13}$CO and C$^{18}$O (1–0) cube from the Three-mm Ultimate Mopra Milky Way Survey (ThrUMMS) survey (Barnes et al. 2015).

## 3. Analysis

### 3.1. Clumps in RCW 106 Cloud Complex

#### 3.1.1. Clump Identification

Figure 1 shows prominent large-scale structures that are comprised of clumpy substructures. The cloud complex has a global elongation angle in PA ~25.0°, slightly different from the Galactic plane angle of ~45°.

We identify the clumpy structures with the *astrodendro* package[9] (Rosolowsky et al. 2008). The *astrodendro* is an unsupervised hierarchical clustering method that builds up a cluster in a tree-like structure where each node represents a leaf, a structure that has no substructure, or a branch, a structure

that has a successor structure. It also computes physical properties of detected leaves that we regard as clumps (e.g., $S$: leaf area, $\sum_S N_{\mathrm{H_2}}$: sum of $N_{\mathrm{H_2}}$ over $S$).

Because the background column density gradually increases from south to north, i.e., approaching the Galactic plane, we separated the cloud complex into three regions: north, center, and south. We estimated the background level $N_{\mathrm{min}}$ (minimum value to be considered) in each region as the flattest and lowest column density levels, which are $8.0 \times 10^{21}$ cm$^{-2}$, $6.0 \times 10^{21}$ cm$^{-2}$, and $4.0 \times 10^{21}$ cm$^{-2}$ for north, center, and south, respectively. We set 60 pixels, corresponding to $1.5 \times 18''$, as the minimum number of pixels needed to define a structure as a leaf. We set $2 \times 10^{21}$ cm$^{-2}$ as the minimum delta parameter (minimum height to be defined as a leaf), which is roughly five times the dispersion of $N_{\mathrm{H_2}}$ measured in the deemed background areas, not to detect too small structures ($\lesssim 30\,M_\odot$). We calculated the mean column densities ($\overline{N}_{\mathrm{H_2}} = \sum_S N_{\mathrm{H_2}}/S$) for each leaf. For analysis, we included only the clumps with $\overline{N}_{\mathrm{H_2}} - N_{\mathrm{min}} > 7.0 \times 10^{21}$ cm$^{-2}$, which is the threshold of the regions in which cores can form (Könyves et al. 2015), and assigned their mean net column densities as $\overline{N}_{\mathrm{net}} = \overline{N}_{\mathrm{H_2}} - N_{\mathrm{min}}$. We calculated its sphere-equivalent radius as $R = \sqrt{S/\pi}$. Then, the mass and mean volume density are evaluated as $M = \mu m_{\mathrm{H}} \overline{N}_{\mathrm{net}} S$ and $\rho = (3/4R)\mu m_{\mathrm{H}} \overline{N}_{\mathrm{net}}$, respectively. The $R$ range is ~0.46–2.29 pc and the mean $R$ is $0.77 \pm 0.32$ pc. The $M$ range is ~230–10600 $M_\odot$ (Table 1).

#### 3.1.2. Star-forming Properties of Clumps

We search for signs of star formation in clumps via the existence of mid-IR emission using the AllWISE source catalog (Wright et al. 2010) and the *Spitzer* 24 μm images for clumps without AllWISE sources. For clumps without any 24 μm point source, we adopted three times the sum of standard deviation within 13″ from the clump center as the detection limit. We classified the clumps into three groups: mid-IR bright clumps that have AllWISE sources, mid-IR faint clumps that are detected only in *Spitzer* emission, and mid-IR quiet clumps that have neither detection.

To understand the star formation activities of the clumps, we estimate their bolometric luminosities $L_{\mathrm{bol}}$ (Table 1), because they are direct scales of the star formation rates (Inoue et al. 2000). $L_{\mathrm{bol}}$ of AllWISE sources associated with the clumps are estimated based on the 12 and 22 μm flux from the AllWISE catalog and on the 70 and 160 μm flux from the PACS Point Source Catalog, following Chen et al. (1995). $L_{\mathrm{bol}}$ of bright sources that are saturated on the *Spitzer* 24 μm or *WISE* 22 μm images are estimated based on the IRAS point-source flux using the method of Carpenter et al. (2000). For sources undetected in 70 or 160 μm, we use $F_{\mathrm{mid\text{-}IR}}$ as the proxy because we found a linear relation $\log_{10}(L_{\mathrm{bol}}/L_\odot) = (0.60 \pm 0.08) \times \log_{10}(F_{\mathrm{mid\text{-}IR}}/\mathrm{Jy}) + (3.3 \pm 0.1)$ with a linear fitting for the sources whose $L_{\mathrm{bol}}$ were estimated. The source with a luminosity of $\gtrsim 10^{3.8}\,L_\odot$ is considered to be a massive B2-type star or more massive (Stahler & Palla 2005).

### 3.2. Magnetic Field in Clumps

#### 3.2.1. Polarization Vectors

In this Letter, we derive only the polarization vector map in $H$ band because it detected most sources associated with RCW 106 among the three bands.
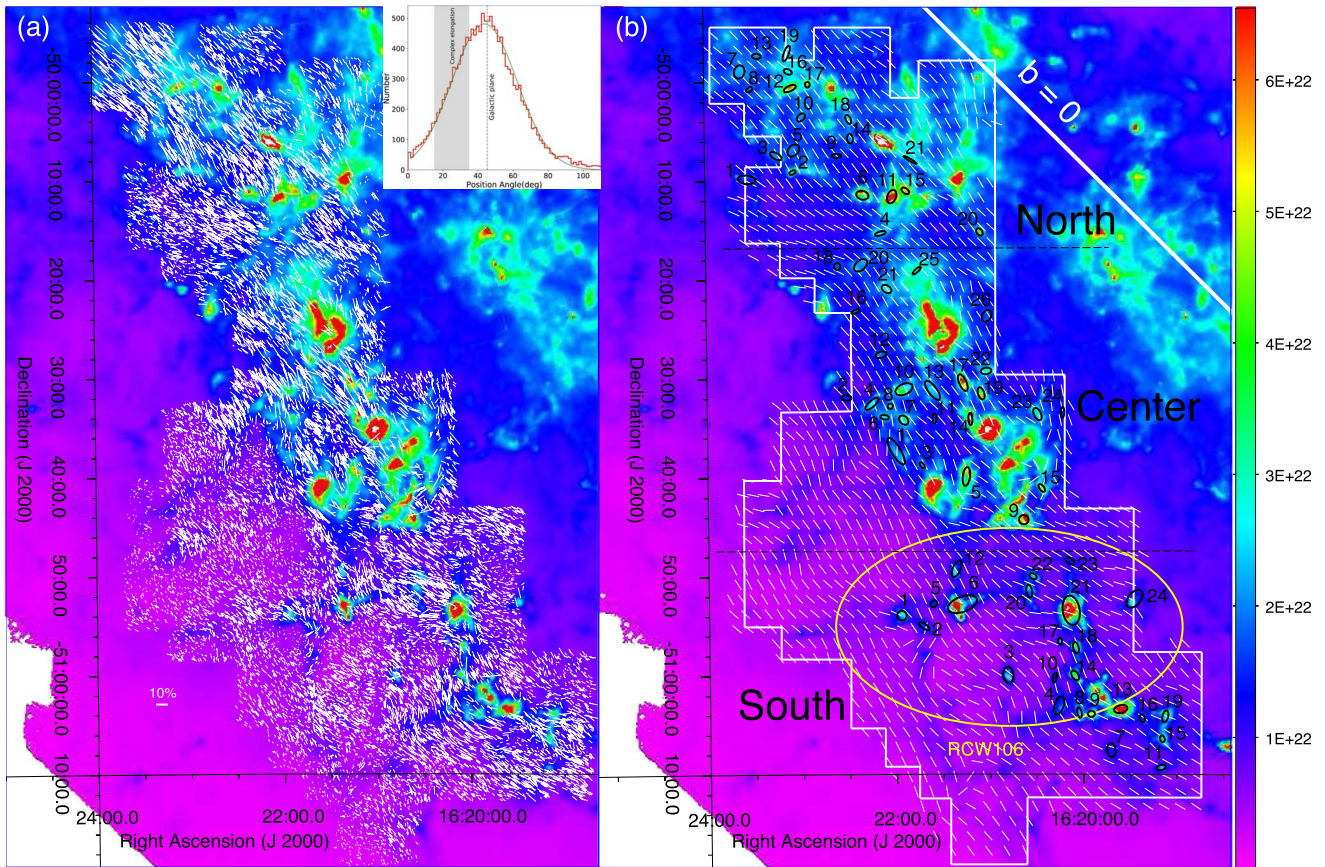
---

[9] https://dendrograms.readthedocs.io/en/stable/index.html

**Figure 1.** (a) *H*-band polarization vector map overlaid on the $N_{H_2}$ map. The histogram of the *H*-band polarization angles is shown in the upper right with a Gaussian fitting line (green line). (b) The average angles of the *H*-band vectors within the $3' \times 3'$ square with a grid spacing of $1'.5$ are shown on the $N_{H_2}$ map. Black ellipses with identification numbers, a yellow ellipse, and a white polygon show *astrodendro* clumps, the extent of the RCW 106 H II region, and the area of our near-IR polarimetry, respectively.

First, on the $P_H$ versus $(H - K_s)$ diagram (Figure 2(a)), we determined the upper limit to remove outlier sources with too high polarizations, such as stars with intrinsic polarization or polarization due to scattering off nebulosity (e.g., Jones 1989), using only the sources with good polarization accuracy ($\Delta P \leqslant 0.3\%$). We approximately estimated an upper threshold line to separate the outliers from the good measurements (a dashed line with a slope of 8.2). The expected background source colors $(H - K_s)_0$ without the reddening by the RCW 106 cloud have a range of $(H - K_s)_0 \sim 0.3$–1.0 (the model of Galactic IR point sources; Wainscoat et al. 1992). We defined the upper limit as the linear line with a slope of 8.2 and passing through the point of $(H - K_s = 0.3, P = 0)$. Thus, we selected only the sources with polarization degree $P_H \leqslant 8.2[(H - K_s) - 0.3]$ and $P/\Delta P \geqslant 3$ (i.e., $\Delta\theta \lesssim 10°$) for analysis. The sources of the concentration at the lower left part of Figure 2(a) appear to be foreground sources and mostly have optical counterparts in the DSS2 red image. To remove the influence of foreground polarization, we estimated the mean $q'$ and $u'$ of these foreground sources with $d = 3.0$–3.5 kpc (referred from *Gaia* DR2; Gaia Collaboration 2018) and subtracted them from the $q'$ and $u'$ of the selected sources.

Second, considering $(H - K_s)_0 = 0.3$–1.0 and the errors of $E(H - K_s) = [(H - K_s) - (H - K_s)_0]$, we include only the sources that have their $H - K_s$ excesses consistent with the $N_{H_2}$ (red dots on Figure 2(b)), within a factor of 2 that is the $N_{H_2}$ uncertainty, which originates from $\kappa_\nu$ (Konyves et al. 2010). The sources with too high $N_{H_2}$ against their $E(H - K_s)$ would

be foreground sources, while those with too low $N_{H_2}$ would not sample the magnetic field of RCW 106. To calculate the column densities expected by the $E(H - K_s)$, we use the equations $E(H - K_s) = 0.065A_v$ (Cohen et al. 1981) and $N_E = 1.0 \times 10^{21}A_v$ (Lacy et al. 2017), i.e., $N_E = 1.54 \times 10^{22}[(H - K_s) - (H - K_s)_0]$ in units of $cm^{-2}$.

We present the *H*-band polarization vectors of the sources that meet the above criteria in Figure 1. The polarization vectors indicate that the global magnetic field direction seems to be nearly parallel to the Galactic plane and the global cloud elongation. The vector angle distribution was determined to be $43°.7 \pm 18°.7$ with a Gaussian fit, of which the peak well agrees with the position angle of the Galactic plane.

### 3.2.2. Magnetic Strength of Clumps

We derived the plane of the sky (POS) magnetic field strength $B$ of each clump using the Davis–Chandrasekhar–Fermi method (Davis 1951; Chandrasekhar & Fermi 1953) modified by Ostriker et al. (2001);

$$B = Q\sqrt{4\pi\rho}\frac{\sigma_v}{\sigma_\theta}, \qquad (1)$$

where $\rho$ is the mean volume density of the clump, $\sigma_v$ is the mean velocity dispersion, $\sigma_\theta$ is the angular dispersion of the polarization vectors, and $Q$ is a correction factor of 0.5 ($\sigma_\theta < 25°$), introduced by Ostriker et al. (2001) with their MHD simulations.

**Table 1**
Properties of 71 Clumps Considered for Analysis

| ID | R.A. (2000) (°) | Decl. (2000) (°) | $\overline{N}_\mathrm{net}$ ($10^{22}$ cm$^{-2}$) | $R$ (pc) | $M_\mathrm{cl}$ ($M_\odot$) | $\sigma_v(^{13}\mathrm{CO})$ (km s$^{-1}$) | $\sigma_v(\mathrm{C}^{18}\mathrm{O})$[a] (km s$^{-1}$) | $\sigma_\theta$ (°) | $B$ ($\mu$G) | $F_\mathrm{mid\text{-}IR}$ (Jy) | $\log(L/L_\odot)$ | $\lambda$ | mid-IR Source |
|---|---|---|---|---|---|---|---|---|---|---|---|---|---|
| N1 | 245.890 | −50.164 | 1.52 | 1.00 | 1061 | 7.66 | 4.28 | 10.75 | 538 | 7.826 | 3.84[b] | 0.38 | bright |
| N2 | 245.769 | −50.152 | 2.96 | 0.46 | 440 | 2.46 | 1.37 | 5.63 | 677 | <0.017 | <2.24[c] | 0.59 | ... |
| N3 | 245.813 | −50.124 | 1.89 | 0.81 | 862 | 3.22 | 1.80 | 4.05 | 745 | 3.025 | 3.59[b] | 0.34 | bright |
| N4 | 245.539 | −50.256 | 2.54 | 0.50 | 453 | 2.55 | 1.43 | 11.16 | 315 | 5.921 | 3.76[b] | 1.09 | bright |
| N5 | 245.767 | −50.115 | 1.80 | 0.87 | 960 | 3.09 | 1.72 | 5.02 | 539 | <0.048 | <2.51[c] | 0.45 | ... |
| N6 | 245.586 | −50.191 | 3.41 | 1.01 | 2431 | 3.63 | 2.03 | 5.02 | 815 | 0.469 | 3.10[b] | 0.56 | bright |
| N7 | 245.906 | −49.982 | 2.12 | 0.94 | 1307 | 3.70 | 2.07 | 5.12 | 665 | 0.015 | 2.21[b] | 0.43 | bright |
| N8 | 245.881 | −50.012 | 1.81 | 0.50 | 313 | 3.28 | 1.83 | 2.43 | 1575 | <0.035 | <2.43[c] | 0.15 | ... |
| N9 | 245.653 | −50.125 | 1.66 | 0.50 | 287 | 2.69 | 1.50 | 9.20 | 327 | <0.019 | <2.27[c] | 0.68 | ... |
| N10 | 245.746 | −50.060 | 2.04 | 0.55 | 432 | 2.55 | 1.42 | 6.10 | 492 | <0.024 | <2.33[c] | 0.56 | ... |
| N11 | 245.509 | −50.194 | 5.87 | 0.85 | 2953 | 1.94 | 1.08 | 12.27 | 254 | <0.018 | <2.25[c] | 3.11 | ... |
| N12 | 245.774 | −50.011 | 4.06 | 0.80 | 1825 | 2.69 | 1.50 | 5.65 | 657 | 0.047 | 2.51[b] | 0.83 | bright |
| N13 | 245.861 | −49.956 | 1.98 | 0.60 | 492 | 3.16 | 1.77 | 4.19 | 843 | <0.016 | <2.22[c] | 0.32 | ... |
| N14 | 245.618 | −50.096 | 2.10 | 0.54 | 420 | 1.55 | 0.86 | 11.61 | 161 | <3.644 | <3.64[c] | 1.75 | ... |
| N15 | 245.473 | −50.184 | 4.92 | 0.59 | 1201 | 2.21 | 1.24 | 7.80 | 501 | <0.130 | <2.77[c] | 1.32 | ... |
| N16 | 245.779 | −49.983 | 2.70 | 0.52 | 501 | 2.94 | 1.64 | 8.17 | 505 | <0.037 | <2.44[c] | 0.72 | ... |
| N17 | 245.728 | −50.005 | 3.74 | 0.48 | 611 | 2.93 | 1.63 | 9.40 | 531 | <0.025 | <2.34[c] | 0.95 | ... |
| N18 | 245.622 | −50.063 | 2.39 | 0.58 | 570 | 1.31 | 0.73 | 3.89 | 418 | <0.041 | <2.47[c] | 0.77 | ... |
| N19 | 245.783 | −49.952 | 2.57 | 0.68 | 821 | 2.59 | 1.45 | 2.40 | 1292 | <0.032 | <2.40[c] | 0.27 | ... |
| N20 | 245.278 | −50.254 | 2.55 | 0.66 | 765 | 1.18 | 0.66 | 3.85 | 370 | 14.573 | 4.00[b] | 0.93 | bright |
| N21 | 245.460 | −50.132 | 2.92 | 0.50 | 505 | 2.66 | 1.49 | 11.50 | 343 | <0.024 | <2.32[c] | 1.15 | ... |
| C1 | 245.500 | −50.622 | 1.83 | 1.37 | 2405 | 2.64 | 1.48 | 12.63 | 148 | <0.100 | <2.70[c] | 1.67 | ... |
| C2 | 245.631 | −50.532 | 1.32 | 0.65 | 392 | 2.19 | 1.22 | 4.07 | 467 | 0.641 | 3.18[b] | 0.38 | bright |
| C3 | 245.431 | −50.646 | 1.95 | 0.47 | 304 | 2.97 | 1.66 | 12.05 | 307 | <0.112 | <2.73[c] | 0.86 | ... |
| C4 | 245.563 | −50.542 | 2.14 | 0.85 | 1088 | 2.38 | 1.33 | 6.65 | 348 | <0.116 | <2.74[c] | 0.83 | ... |
| C5 | 245.314 | −50.665 | 3.97 | 0.96 | 2558 | 2.09 | 1.17 | 16.83 | 154 | 284.421 | 4.77[b] | 3.46 | bright |
| C6 | 245.530 | −50.565 | 2.28 | 0.53 | 451 | 2.28 | 1.27 | 16.09 | 179 | <0.139 | <2.79[c] | 1.72 | ... |
| C7 | 245.480 | −50.570 | 2.57 | 0.81 | 1173 | 2.71 | 1.51 | 13.20 | 224 | <0.337 | <3.02[c] | 1.54 | ... |
| C8 | 245.515 | −50.547 | 2.28 | 0.48 | 361 | 2.48 | 1.39 | 9.25 | 359 | <0.544 | <3.14[c] | 0.85 | ... |
| C9 | 245.162 | −50.738 | 4.57 | 0.88 | 2467 | 2.81 | 1.57 | 21.88 | 179 | 17.716 | 4.05[b] | 3.43 | bright |
| C10 | 245.479 | −50.518 | 2.43 | 1.26 | 2682 | 3.10 | 1.73 | 7.78 | 339 | <0.083 | <2.65[c] | 0.96 | ... |
| C11 | 245.398 | −50.567 | 1.51 | 0.55 | 321 | 3.86 | 2.16 | 8.91 | 441 | <0.275 | <2.96[c] | 0.46 | ... |
| C12 | 245.539 | −50.460 | 1.66 | 0.72 | 605 | 3.24 | 1.81 | 6.28 | 480 | <0.320 | <3.00[c] | 0.47 | ... |
| C13 | 245.403 | −50.520 | 2.23 | 1.08 | 1827 | 3.94 | 2.20 | 15.62 | 222 | <1.439 | <3.39[c] | 1.36 | ... |
| C14 | 245.303 | −50.569 | 5.61 | 0.55 | 1178 | 3.43 | 1.91 | 10.83 | 621 | <0.917 | <3.28[c] | 1.22 | ... |
| C15 | 245.114 | −50.685 | 3.57 | 0.60 | 897 | 2.90 | 1.62 | 24.79 | 174 | 38.016 | 4.25[b] | 2.76 | bright |
| C16 | 245.606 | −50.387 | 1.64 | 0.49 | 280 | 3.57 | 1.99 | 9.94 | 400 | 0.050 | 2.52[b] | 0.55 | faint |
| C17 | 245.323 | −50.508 | 3.55 | 1.07 | 2826 | 2.76 | 1.54 | 6.78 | 454 | 8.936 | 3.87[b] | 1.05 | bright |
| C18 | 245.653 | −50.311 | 1.68 | 0.60 | 421 | 3.96 | 2.21 | 11.71 | 346 | <0.220 | <2.91[c] | 0.65 | ... |
| C19 | 245.274 | −50.526 | 2.99 | 0.83 | 1447 | 3.75 | 2.09 | 16.05 | 271 | <0.379 | <3.05[c] | 1.49 | ... |
| C20 | 245.591 | −50.309 | 1.95 | 1.06 | 1521 | 2.67 | 1.49 | 3.40 | 654 | 0.387 | 3.05[b] | 0.40 | bright |
| C21 | 245.523 | −50.349 | 2.52 | 0.78 | 1063 | 3.82 | 2.14 | 6.44 | 655 | 0.069 | 2.60[b] | 0.52 | faint |
| C22 | 245.261 | −50.488 | 2.53 | 0.73 | 952 | 3.14 | 1.75 | 15.03 | 238 | 3.113 | 3.60[b] | 1.44 | bright |
| C23 | 245.125 | −50.561 | 2.43 | 0.87 | 1280 | 2.54 | 1.42 | 7.92 | 329 | 5.219 | 3.73[b] | 1.00 | bright |
| C24 | 245.059 | −50.558 | 1.42 | 0.49 | 242 | 3.41 | 1.91 | 11.52 | 307 | <0.062 | <2.57[c] | 0.62 | ... |
| C25 | 245.444 | −50.319 | 3.17 | 0.49 | 541 | 4.95 | 2.76 | 4.88 | 1573 | 0.229 | 2.92[b] | 0.27 | bright |
| C26 | 245.260 | −50.395 | 1.59 | 0.89 | 887 | 3.45 | 1.93 | 9.27 | 304 | <3.432 | <3.62[c] | 0.70 | ... |
| S1 | 245.487 | −50.899 | 1.82 | 0.86 | 946 | 2.61 | 1.46 | 10.49 | 222 | <0.086 | <2.66[c] | 1.11 | ... |
| S2 | 245.427 | −50.917 | 1.57 | 0.66 | 478 | 3.00 | 1.67 | 9.79 | 289 | <0.054 | <2.54[c] | 0.73 | ... |
| S3 | 245.203 | −51.000 | 1.12 | 1.29 | 1299 | 2.47 | 1.38 | 8.98 | 157 | 1.167 | 3.34[b] | 0.96 | bright |
| S4 | 245.067 | −51.051 | 1.46 | 0.97 | 962 | 2.00 | 1.12 | 8.68 | 173 | 3.212 | 3.60[b] | 1.14 | bright |
| S5 | 245.401 | −50.879 | 1.15 | 0.61 | 299 | 2.84 | 1.58 | 8.17 | 291 | 1.736 | 3.44[b] | 0.53 | bright |
| S6 | 245.325 | −50.880 | 2.53 | 1.86 | 6123 | 3.38 | 1.89 | 11.47 | 210 | 18.896 | 4.07[b] | 1.62 | bright |
| S7 | 244.927 | −51.126 | 1.11 | 0.92 | 649 | 2.36 | 1.32 | 9.88 | 161 | <0.073 | <2.62[c] | 0.93 | ... |
| S8 | 245.013 | −51.063 | 2.13 | 0.61 | 552 | 2.08 | 1.16 | 8.34 | 285 | 5.675 | 3.75[b] | 1.01 | bright |
| S9 | 244.981 | −51.065 | 2.56 | 0.62 | 687 | 1.90 | 1.06 | 6.80 | 347 | 13.061 | 3.97[b] | 0.99 | bright |
| S10 | 245.079 | −51.004 | 1.19 | 0.52 | 226 | 2.06 | 1.15 | 10.79 | 176 | 0.422 | 3.08[b] | 0.91 | faint |
| S11 | 244.792 | −51.155 | 1.48 | 0.66 | 452 | 1.81 | 1.01 | 9.55 | 174 | <0.053 | <2.54[c] | 1.15 | ... |
| S12 | 245.340 | −50.821 | 1.55 | 0.94 | 957 | 3.00 | 1.68 | 16.30 | 145 | 1.094 | 3.32[b] | 1.44 | bright |
| S13 | 244.902 | −51.057 | 5.04 | 1.01 | 3568 | 2.38 | 1.33 | 16.21 | 201 | 657.000 | 4.99[d] | 3.38 | bright |
| S14 | 245.024 | −51.000 | 2.68 | 0.73 | 1001 | 1.51 | 0.85 | 11.28 | 157 | 1.760 | 3.45[b] | 2.30 | bright |
| S15 | 244.790 | −51.107 | 2.81 | 0.51 | 508 | 1.73 | 0.97 | 14.42 | 173 | 4.466 | 3.69[b] | 2.19 | bright |

**Table 1**
(Continued)

| ID | R.A. (2000) (°) | Decl. (2000) (°) | $\overline{N}_{\mathrm{net}}$ $(10^{22}\ \mathrm{cm}^{-2})$ | $R$ (pc) | $M_{\mathrm{cl}}$ $(M_{\odot})$ | $\sigma_v(^{13}\mathrm{CO})$ $(\mathrm{km\ s}^{-1})$ | $\sigma_v(\mathrm{C}^{18}\mathrm{O})^{a}$ $(\mathrm{km\ s}^{-1})$ | $\sigma_\theta$ (°) | $B$ $(\mu G)$ | $F_{\mathrm{mid\text{-}IR}}$ (Jy) | $\log(L/L_{\odot})$ | $\lambda$ | mid-IR Source |
|---|---|---|---|---|---|---|---|---|---|---|---|---|---|
| S16 | 244.844 | −51.072 | 1.61 | 0.50 | 282 | 1.75 | 0.98 | 15.91 | 120 | <0.018 | <2.26[c] | 1.80 | ... |
| S17 | 245.065 | −50.943 | 1.51 | 0.49 | 251 | 3.96 | 2.21 | 17.84 | 240 | <3.759 | <3.65[c] | 0.85 | ... |
| S18 | 245.022 | −50.954 | 2.50 | 0.72 | 897 | 2.62 | 1.46 | 15.68 | 191 | <1.874 | <3.46[c] | 1.76 | ... |
| S19 | 244.783 | −51.069 | 2.86 | 0.65 | 836 | 1.32 | 0.74 | 14.55 | 117 | 30.058 | 4.19[b] | 3.30 | bright |
| S20 | 245.147 | −50.859 | 1.97 | 0.69 | 650 | 2.12 | 1.18 | 9.14 | 241 | 2.924 | 3.58[b] | 1.11 | bright |
| S21 | 245.035 | −50.891 | 2.87 | 2.29 | 10557 | 2.80 | 1.57 | 12.50 | 153 | 580.714 | 4.96[d] | 2.52 | bright |
| S22 | 245.137 | −50.834 | 2.05 | 0.59 | 506 | 2.38 | 1.33 | 6.14 | 442 | 0.420 | 3.07[b] | 0.63 | bright |
| S23 | 245.039 | −50.808 | 1.24 | 0.64 | 351 | 3.55 | 1.98 | 13.93 | 218 | <0.947 | <3.29[c] | 0.77 | ... |
| S24 | 244.866 | −50.871 | 1.30 | 1.40 | 1781 | 1.56 | 0.87 | 8.60 | 106 | 0.560 | 3.15[b] | 1.64 | bright |

**Notes.**
[a] Estimated from the average ratio of the $\sigma_v(^{13}\mathrm{CO})/\sigma_v(\mathrm{C}^{18}\mathrm{O})$.
[b] Estimated from the 12 and 22 $\mu$m fluxes (AllWISE) and the PACS 70 and 160 $\mu$m fluxes (Chen et al. 1995).
[c] Estimated from the linear relation; $\log_{10}(L_{\mathrm{bol}}/L_{\odot}) = (0.60 \pm 0.08) \times \log_{10}(F_{\mathrm{mid\text{-}IR}}/\mathrm{Jy}) + (3.3 \pm 0.1)$. See Section 3.1.2.
[d] Estimated from the IRAS fluxes 12, 25, and 60 $\mu$m (Carpenter et al. 2000).
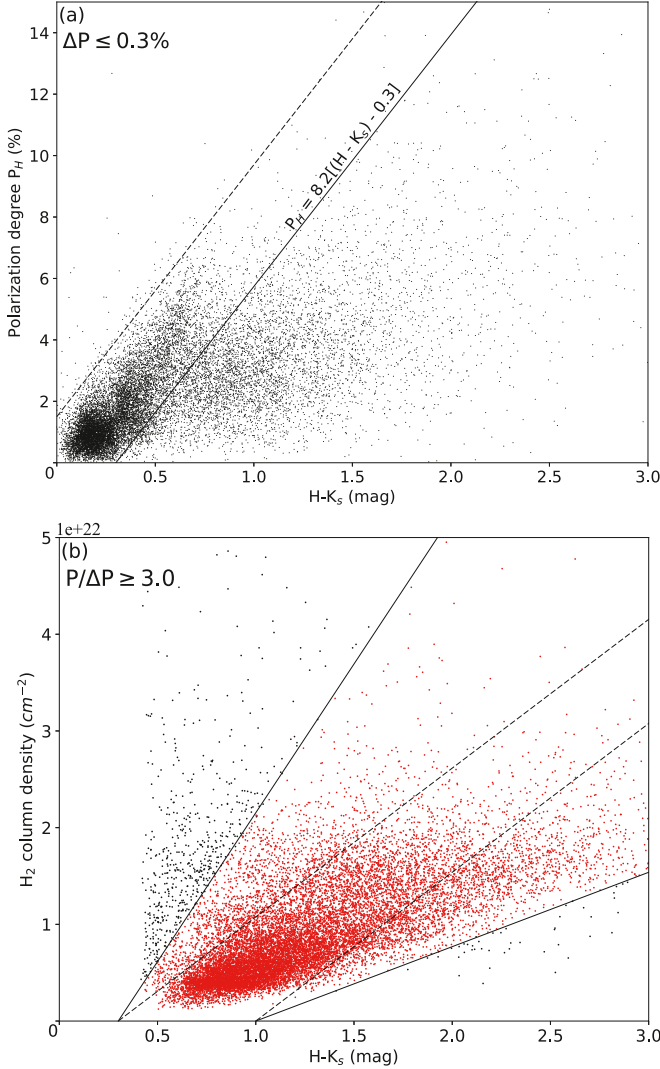


**Figure 2.** (a) Polarization degree vs. $H - K$s magnitude diagram for good polarimetric sources with $\Delta P \leqslant 0.3\%$. The solid line, which has the same slope as the dashed line, is our determined upper limit. See the details in Section 3.2.1. Here, we adopted $E(H - K_{\mathrm{s}}) = 0.065 A_v$ (Cohen et al. 1981). (b) H$_2$ column density vs. $H - K_{\mathrm{s}}$ color for the sources that are below our upper limit and have $P$ of $P/\Delta P \geqslant 3$. The dashed lines are the H$_2$ column densities expected from the color excess. See more details in Section 3.2.1.

We applied a single Gaussian fit to the $^{13}$CO cube data in the range of $V_{\mathrm{LSR}} = -80$ to $-30$ km s$^{-1}$ to determine the velocity dispersion $\sigma_v$ at each position of the $^{13}$CO cube data and obtained the mean $\sigma_v$ within each clump. For some clumps that have double peaks, double Gaussian fits were applied to the integrated $^{13}$CO spectra. Because $^{13}$CO might sample not only clump but also inter-clump materials, we correct $\sigma_v$ by dividing by the mean $\sigma_v(^{13}\mathrm{CO})/\sigma_v(\mathrm{C}^{18}\mathrm{O})$. We derived the mean $\sigma_v(^{13}\mathrm{CO})/\sigma_v(\mathrm{C}^{18}\mathrm{O})$ by taking only pixels that are detected in both lines ($T_{\mathrm{peak}} > 1.0$ K). Consequently, we obtained $\langle \sigma_v(^{13}\mathrm{CO})/\sigma_v(\mathrm{C}^{18}\mathrm{O}) \rangle = 1.76 \pm 0.55$.

To derive the angular dispersion $\sigma_\theta$ of the $H$-band polarization vectors, we adopted the method of Hildebrand et al. (2009). The angular difference is given as $\Delta\theta(l) \equiv \theta(x) - \theta(x + l)$, between the $N(l)$ pairs of vectors separated by the displacement $l$. The square of the angular dispersion function (ADF; see also Kobulnicky et al. 1994) is expressed as follows:

$$\langle \Delta\theta^2(l) \rangle \equiv \frac{1}{N(l)} \sum_{i=1}^{N(l)} [\theta(x) - \theta(x + l)]^2, \qquad (2)$$

and can be approximated as follows:

$$\langle \Delta\theta^2(l) \rangle_{\mathrm{tot}} \simeq b^2 + m^2 l^2 + \sigma_{\mathrm{M}}^2(l), \qquad (3)$$

where $b$, $m$, and $\sigma_{\mathrm{M}}(l)$ present the contributions of the turbulent dispersion, large-scale structure, and measurement uncertainties, respectively.

We constructed the plot of squared ADF and $l$ and fit Equation (3) to derive $b$ and $m$ (Chapman et al. 2011), toward the clump and its immediate surroundings. Following Hildebrand et al. (2009), we calculated $\sigma_\theta$ approximately as the ratio of the turbulent to large-scale magnetic field strength;

$$\sigma_\theta = \frac{\langle B_{\mathrm{t}}^2 \rangle^{1/2}}{B_0} = \frac{b}{\sqrt{2 - b^2}}, \qquad (4)$$

where $B_0$ is a large-scale magnetic field, and $B_{\mathrm{t}}$ is a turbulent component. See the details in Section 3 of Hildebrand et al. (2009).

We used the $H$-band vectors within $2'$, $\sim$2–3 times the clump $R$, from the clump center to make the fit. To avoid bad fitting, the clumps with the number of vectors <30 were excluded. We
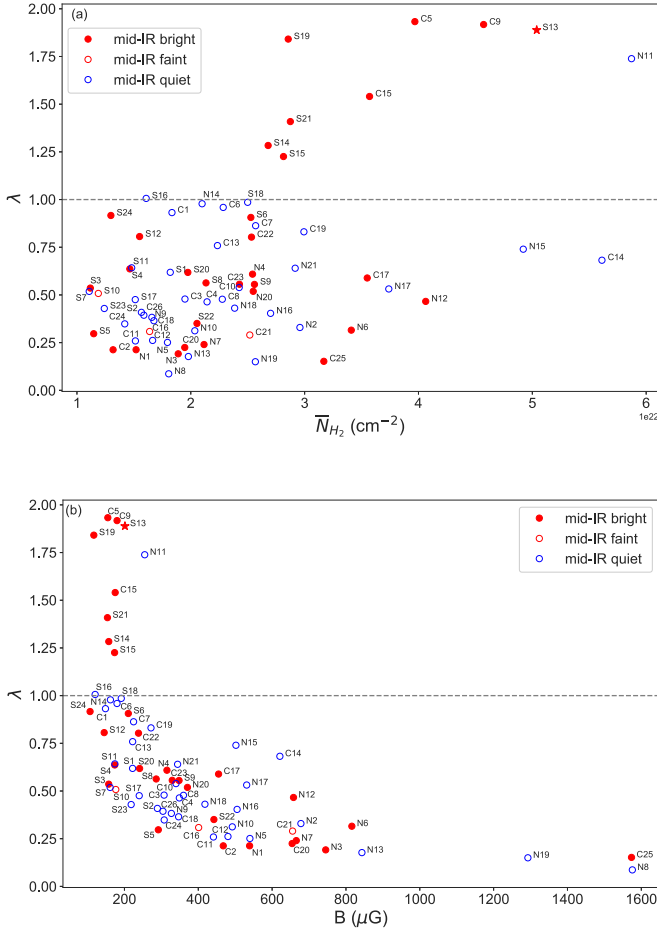
**Figure 3.** Normalized mass-to-flux ratio $\lambda$ vs. (a) mean column density, and (b) magnetic field strengths.

exclude the clumps that have bad fits even if they have more than 30 vectors. Seventy-one clumps are left for further analysis. We note that several clumps in the very high density areas are not included because the number of vectors of the background sources does not satisfy our selection criterion. Finally, we obtain the magnetic field strengths of $\sim$100–1600 $\mu$G for 71 clumps.

While Jones et al. (2015) found that grain alignment becomes a problem at $A_{\rm v} \gtrsim 20$ in starless cores, Whittet et al. (2008) suggested alignment enhancement around the embedded stars. Since the mid-IR bright clumps have embedded stars, such enhancement might have occurred and our analysis would be valid. Note that mid-IR quiet clumps have smaller R compared to the bright ones and that there is a possibility that we do not properly estimate their magnetic fields, but rather their exterior's.

## 4. Discussion and Conclusion

### 4.1. Magnetic Stability of Clumps in RCW 106

Magnetic field strengths derived from our measurements of the clumps in RCW 106 are about 100–1600 $\mu$G and the distribution of the magnetic field strength $B$ is not much different among the different clump classes (Table 1 and Figure 3). As mentioned in Section 1, Shu et al. (1987) predicted that the process of massive star formation is different from low-mass star formation. Magnetic fields in magnetically

subcritical clumps prevent the clumps from collapsing gravitationally under conservation of magnetic flux. Magnetically supercritical clumps would generate the high-mass core needed for massive star formation because massive stars might require drastic collapsing.

For a clump, the magnetic stability is quantifiable as the mass-to-magnetic-flux ratio $\lambda_{\rm obs}$ as

$$\lambda_{\rm obs} = \frac{\mu m_{\rm H} \overline{N}_{\rm net}}{B} \qquad (5)$$

or the normalized mass-to-magnetic flux ratio as

$$\lambda = \frac{\lambda_{\rm obs}}{\lambda_{\rm crit}}, \qquad (6)$$

where $\lambda_{\rm crit} = 1/\sqrt{4\pi^2 G}$ is the stability criterion (Nakano & Nakamura 1978). The clump is magnetically stable if $\lambda$ is equal to or less than 1, otherwise unstable.

Sixty-two of the clumps are close to the critical condition or under the subcritical condition ($\lambda \lesssim 1$) and $\lambda$ increases linearly with $\overline{N}_{\rm net}$, but inversely correlates with $B$ as expected (Figure 3). Almost all (36/37) mid-IR quiet clumps have $\lambda \lesssim 1$ and only the clump N11 has larger $\lambda$ of $>1$. More than half (23/31) of the active star-forming (mid-IR bright) clumps are close to magnetically critical or subcritical, while 8 clumps are supercritical ($\lambda > 1$).

We examined the correlation between $\lambda$ with $F_{\rm mid\text{-}IR}$ and $M_{\rm clump}/M_{\rm virial}$ in order to examine the relation between magnetic field instability with star formation activities and gravitational instability. $\lambda$ correlates almost linearly with $\log_{10}(F_{\rm mid\text{-}IR}/{\rm Jy})$ and $M_{\rm clump}/M_{\rm virial}$ (Figure 4). The interesting feature is that the mid-IR *brighter* clumps tend to be magnetically supercritical (Figure 4(a)), especially the clumps with luminosity $\gtrsim 10^{3.8}\,L_{\odot}$ (flux $\gtrsim 10\,{\rm Jy}$), which are classified as the massive star-forming clumps ($\gtrsim 800\,M_{\odot}$). These facts suggest that massive stars tend to be formed in magnetically supercritical clumps. Figure 4(b) shows that mid-IR bright, or massive star-forming clumps are mostly magnetically and gravitationally unstable.

#### 4.1.1. Implication of Magnetic Fields on Massive Star Formation in RCW 106

Our results strongly suggest that massive star formation prefers to occur inside magnetically and gravitationally unstable clumps. The latter point is consistent with previous studies, both in observations (Nguyen-Luong et al. 2016) and simulation (Howard et al. 2016). They claimed that massive star formation occurs in a gravitationally unstable cloud complex rather than in a stable one. We therefore propose a new criterion for identifying massive star-forming clumps, which is:

$$\text{Massive star forming clumps} \iff \begin{cases} \frac{M_{\rm clump}}{M_{\rm virial}} > 1, \text{ gravitationally unstable} \\ \frac{\lambda_{\rm obs}}{\lambda_{\rm crit}} > 1, \text{ magnetically unstable.} \end{cases}$$

Massive star-forming clumps are therefore lying in the upper right of Figure 4. Our results imply that massive star formation could more quickly occur in the magnetically unstable clumps. These suggest the importance of the process that enhances the clump density while not increasing the magnetic flux for massive star formation, e.g., the buildup of molecular gas along the magnetic field. Naturally, supercritical clumps will arise in
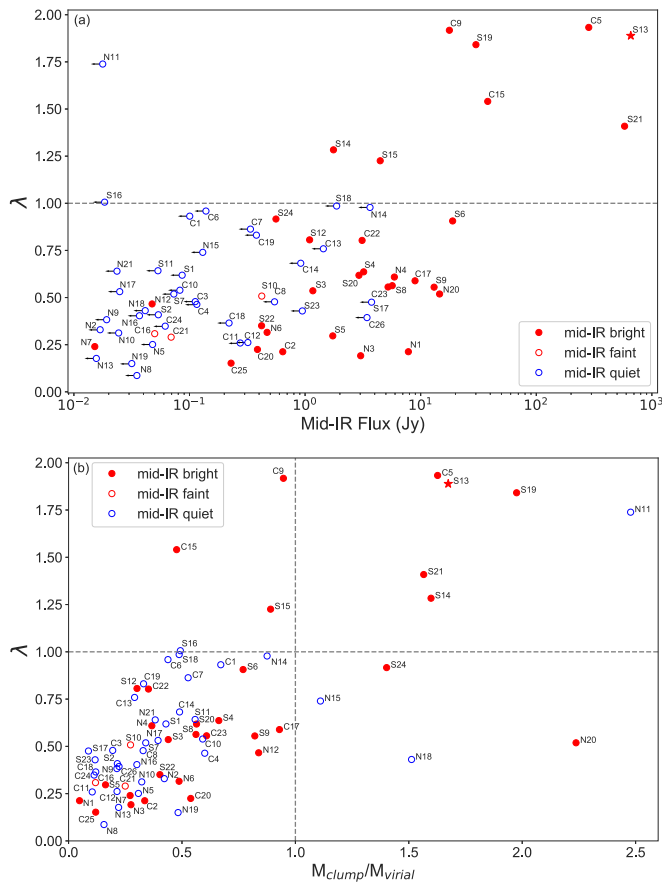
**Figure 4.** Normalized mass-to-flux ratio vs. (a) mid-IR flux and (b) $M_{clump}/M_{virial}$. For mid-IR quiet clumps, the upper limits are indicated by small arrows (see the text).

the agglomerated environments of clumps in large cloud complexes (Shu 1987; Shu et al. 1987).

### ORCID iDs

Shohei Tamaoki ● https://orcid.org/0000-0001-9073-2958
Koji Sugitani ● https://orcid.org/0000-0003-3081-6898
Fumitaka Nakamura ● https://orcid.org/0000-0001-5431-2294
Takayoshi Kusune ● https://orcid.org/0000-0002-9218-9319
Makoto Watanabe ● https://orcid.org/0000-0002-3656-4081
Motohide Tamura ● https://orcid.org/0000-0002-6510-0681

### References

Andersson, B. G., Lazarian, A., & Vaillancourt, J. E. 2015, ARA&A, 53, 501
Bains, I., Wong, T., Cunningham, M., et al. 2006, MNRAS, 367, 1609
Barnes, P., Muller, E., Indermuehle, B., et al. 2015, ApJ, 812, 6
Carpenter, J. M., Heyer, M. H., & Snell, R. L. 2000, ApJS, 130, 381
Chandrasekhar, S., & Fermi, E. 1953, ApJ, 118, 113
Chapman, N. L., Goldsmith, P. F., Pineda, J. L., et al. 2011, ApJ, 741, 21
Chen, H., Myers, P. C., Ladd, E. F., & Wood, D. O. S. 1995, ApJ, 445, 377
Cohen, J. G., Frogel, J. A., Persson, S. E., & Elias, J. H. 1981, ApJ, 249, 481
Crutcher, R. M. 2012, ARA&A, 50, 29
Davis, L. 1951, PhRv, 81, 890
Gaia Collaboration 2018, A&A, 616, A1
Hildebrand, R. H., Kirby, L., Dotson, J. L., Houde, M., & Vaillancourt, J. E. 2009, ApJ, 696, 567
Howard, C. S., Pudritz, R. E., & Harris, W. E. 2016, MNRAS, 461, 2953
Inoue, A. K., Hirashita, H., & Kamaya, H. 2000, PASJ, 52, 539
Jones, T. J. 1989, ApJ, 346, 728
Jones, T. J., Bagley, M., Krejny, M., & Andersson, B. G. 2015, AJ, 149, 31
Kandori, R., Kusakabe, N., Tamura, M., et al. 2006, Proc. SPIE, 6269, 159
Kobulnicky, H. A., Molnar, L. A., & Jones, T. J. 1994, AJ, 107, 1433
Könyves, V., André, P., Men'shchikov, A., et al. 2015, A&A, 584, A91
Konyves, V., Andre, Ph., Men'shchikov, A., et al. 2010, A&A, 518, L106
Kusune, T., Sugitani, K., Miao, J., et al. 2015, ApJ, 798, 60
Lacy, J. H., Sneden, C., Kim, H., & Jaffe, T. D. 2017, ApJ, 838, 66
Lo, N., Cunningham, M. R., Jones, P. A., et al. 2009, MNRAS, 395, 1021
Lockman, F. J. 1979, ApJ, 232, 761
Lowe, V., Cunningham, M. R., Urquhart, J. S., et al. 2014, MNRAS, 441, 256
Lynga, G. 1964, MeLuS, 141, 1
Mookerjea, B., Kramer, C., Nielbock, M., & Nyman, L.-Å. 2004, A&A, 426, 119
Nagashima, C., Nagayama, T., Nakajima, Y., et al. 1999, in Star Formation 1999, ed. T. Nakamoto (Nobeyama: Nobeyama Radio Observatory), 397
Nagayama, T., Nagashima, C., Nakajima, Y., et al. 2003, Proc. SPIE, 4841, 459
Nakano, t., & Nakamura, T. 1978, PASJ, 30, 671
Nguyen, H., Nguyen Luong, Q., Martin, P. G., et al. 2015, ApJ, 812, 7
Nguyen-Luong, Q., Nguyen, H. V. V., Motte, F., et al. 2016, ApJ, 833, 23
Ostriker, E. C., Stone, J. M., & Gammie, C. F. 2001, ApJ, 546, 980
Rosolowsky, E. W., Pineda, J. E., Kauffmann, J., & Goodman, A. A. 2008, ApJ, 679, 1338
Shu, F. H. 1987, NASCP, 2466, 743
Shu, F. H., Adams, F. C., & Lizano, S. 1987, ARA&A, 25, 23
Skrutskie, M. F., Cutri, R. M., Stiening, R., et al. 2006, AJ, 131, 1163
Stahler, S. W., & Palla, F. 2005, The Formation of Stars (Weinheim: Wiley-VCH), 865
Wainscoat, R. J., Cohen, M., Volk, K., et al. 1992, ApJS, 83, 111
Wardle, J. F. C., & Kronberg, P. P. 1974, ApJ, 194, 249
Whittet, D. C. B., Hough, J. H., & Lazarian, A. 2008, ApJ, 674, 304
Wong, T., Ladd, E. F., Brisbin, D., et al. 2008, MNRAS, 386, 1069
Wright, E. L., Eisenhardt, P. R. M., Mainzer, A. K., et al. 2010, AJ, 140, 1868